



Force Generation Mechanisms by an Insect Wing in Hovering Motion with Different Flipping Schedules

H. R. Hamdani, A. Aizaz[†] and M. A. Naqvi

College of Aeronautical Engineering, National University of Sciences and Technology, Islamabad, Pakistan

[†]Corresponding Author Email: ahmadaizaz@cae.nust.edu.pk

(Received January 25, 2016; accepted July 20, 2016)

ABSTRACT

The aerodynamic force and the flow structure of a wing performing hovering motion at small Reynolds number ($Re=4000$) is calculated by computationally solving the 3D Navier-Stokes equations. The computations are performed for the hovering motion which consists of stroke 1, followed by the flipping motion for reversing the direction and then the stroke 2 (similar to stroke 1 but in the opposite direction). The intent of the study is to research the effects of different scheduling of the flip motion between the two strokes. At $Re=4000$, the delayed stall mechanism is noted during the azimuth rotation of a wing with a high value of C_L due to stabilized Leading Edge Vortex. The lift contribution during the flip (pitch rotation for reversing the direction) for the complete stroke is not substantial. During a stroke, the wing encountered the wake from the previous stroke in which, the wake does not contribute positively.

Keywords: Hovering; Delayed stall; Wake capture; Flip scheduling; Low Reynolds number; CFD.

NOMENCLATURE

a_∞	speed of sound	M_∞	free stream Mach number
c	mean chord length	Re	Reynolds number
C_D	drag coefficient	U_∞	free-stream reference velocity
$\overline{C_D}$	time averaged drag coefficient	α	angle of attack
CFD	Computational Fluid Dynamics	τ	non-dimensional time
C_L	lift coefficient	τ_a	non-dimensional time for acceleration
$\overline{C_L}$	time averaged lift coefficient	ψ	azimuth rotation angle
l	radial position along the wing length from axis of rotation	$\dot{\psi}$	angular velocity of azimuth rotation
LEV	leading Edge Vortex		

1. INTRODUCTION

Flapping flight of natural flyers has always fascinated the researchers and the curiosity has increased manifold due to interest in developing an electromechanical device capable of mimicking the Flapping-wing insects. The flapping-wing insects employ unsteady aerodynamic mechanisms to keep them afloat, and there have been many studies on this topic such as Ellington (1984a), Ellington (1984b), Ellington (1984c), Ellington (1984d), Ellington *et al.* (1996), Van den Berg and Ellington (1997a), Van den Berg and Ellington (1997b), Dickinson *et al.* (1999), Liu (2002), Liu (2005),

Sane (2003), Lehman (2004a), Lehman (2004b) and Wang (2005). During the last few years, computational fluid dynamics (CFD) has also been widely applied to studies concerning insect flight. For instance, Liu and Kawachi (1998), Liu *et al.* (1998), Sun and Tang (2002a), Sun and Tang (2002b), Wang *et al.* (2004), Liu (2005), Wu and Sun (2004), Sun and Yu (2006), Yanpeng and Sun (2008), Hamdani and Sun (2000), Yilmaz (2011), Jun-Jiang *et al.* (2014) and Bross and Rockwell (2014). A major conclusion from these studies is that the insects obtain a sufficient lift force to support their weight through the vortices generated by the flapping wings. Among the many

mechanisms involved in the insect flight, the “delayed stall” identified by Ellington (1996) and Hamdani (2010), which is featured by a prolonged attachment of a leading-edge vortex (LEV) on a wing, has been widely recognized as an important unsteady aerodynamic mechanism contributing to the enhancement of the lift force generation in the flapping-wing insects. Other unsteady mechanisms might contribute to the force production in the insect flight. Dickinson *et al.* (1999) suggested that the rotational circulation and the wake capture increased the aerodynamic force during the rotational phase of the wing motion. These studies have made significant contributions to the understanding of the different aspects of the aerodynamic mechanisms involved in the insect flight.

Hovering is the condition of staying aloft while having no mean translational motion. It is the most extreme and demanding aspect of the flapping wing flight. The flow over a wing undergoing hovering kinematics is unsteady, such that during one stroke, the wing accelerates and rotates, all the while traveling a distance of only about 3 to 5 chord lengths. Hikaru *et al.* (2008) performed a CFD study of an unsteady 3D near- and far-field vortex wake dynamics in a hovering fruit fly and their relation to the lift force generation using biologically inspired dynamic flight simulator. By comparing the computed results for the hovering Hawkmoth and the Fruit fly, marked dependence of the span-wise flow and the delayed stall on Re is elucidated.

2. THE PRESENT STUDY

In this work, CFD methodology is applied to understand the instantaneous force generation and vortex structures during hovering motion of a Fruit fly wing. Using the solution of the Navier-Stokes equations, the aerodynamic force and the detailed flow structure around the wing are obtained. The results provide a useful insights into the mechanism of the unsteady force generation during the hovering at $Re=4000$. The Reynolds number is chosen since this Re range has been used in many studies for MAVs such as by A Naderi *et al.* (2016). It is pertinent to mention that $Re=4000$ is selected on the premise that the length scale (mean aerodynamic chord) becomes closer to a Micro Air Vehicle (MAV).

Attention is focused on capturing the unsteady aerodynamic effects during the hovering by systematically scheduling the flip motion between the two strokes. The rationale is to investigate the effects of various flip schedules on the performance of the subsequent stroke with a focus on wake capture mechanism. The experimental study by Dickinson *et al.* (1999) has used these scheduling to generate force peaks at the start and the end of the stroke leading to wake capture and rotational lift effects. Numerical analysis by Sun *et al.* (2002a and 2002b) has, as yet, not found any conclusive evidence of wake capture phenomena and has thus, supported the findings of Ellington *et al.* (1996) that

if LEV does not shed, wake capture mechanism might not exist.

3. COMPUTATIONAL METHOD AND GRID GENERATION

3.1 Computational Method

The 3D compressible Navier-Stokes equations are numerically solved in the present study. The Mach number is given a low value such that the solution is a close approximation to that of incompressible flow (further details presented in the next section). For the flow past a body in arbitrary motion, the governing equations can be cast in an inertial frame of reference using a general time-dependent coordinate transformation to account for the motion of the body. Employing this approach, the Navier-Stokes equations are expressed in a strong conservation form. They are well documented in the Beam and Warming (1978) and will not be repeated here.

The Navier-Stokes equations are solved using the implicit, approximate-factorization algorithm of Beam and Warming (1978). The scheme is formulated using the three-point-backward implicit time differencing and the second-order finite difference approximation for all the spatial derivatives. A constant coefficient fourth-order explicit and a second-order implicit spectral damping are added to damp the high frequency oscillations and enhance the stability behavior as described by Steger (1978).

The calculations are performed in the still air. At the wing surface, no slip wall boundary condition is enforced which means that the fluid on the wall surface will move with the same velocity as the wall. Along the grid cut-line, the periodic boundary conditions are enforced. The pressure on the boundary is obtained through the normal component of the momentum equation.

3.2 Grid Generation

A body-fitted O-H-type grid is constructed by span-wise stacking the 2-D O-type grids. The two-dimensional grid is generated by using a special Poisson solver based on the methods of Thomas (1982). A portion of the grid used for the wing in span-wise and chord-wise direction is shown in Fig. 1.

For the stacking procedure, the mid span chord is used to normalize the wing under a 7th order polynomial for the leading edge and a 6th order polynomial for the trailing edge. The resulting wing has a span (B) of 2.5 with the aspect ratio ($AR=B^2/S$) 3.74 (Fig. 2)

4. WING KINEMATICS, GRID AND MACH NUMBER SENSITIVITY

4.1 Model Wing Kinematics

Figure 3 depicts the hovering motion, which consists of stroke 1, stroke reversal (flipping) and

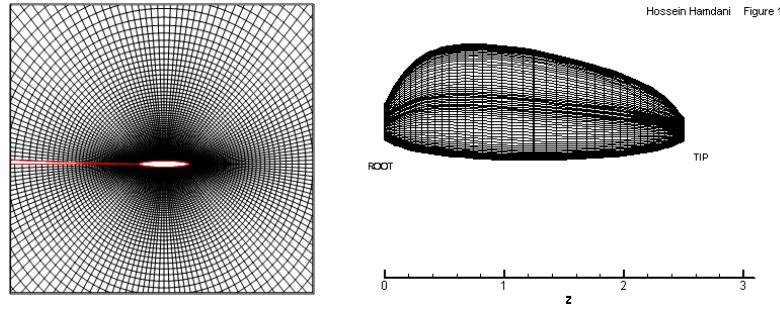


Fig. 1. A portion of the grid around a section and on the wing surface.

the stroke 2. The wing during stroke 1 (translation) performs azimuth rotation around the y-axis. Near the end of stroke 1, the wing decelerates in azimuth rotation in preparation of the stroke 2 which is in opposite direction. Simultaneously the wing performs flipping (pitch rotation) along the spanwise axis for stroke reversal so that angle of attack during Stroke 1 and 2 are same.

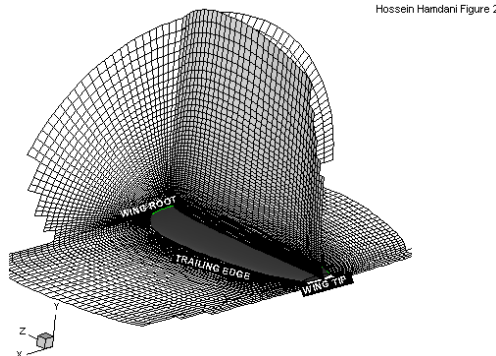


Fig. 2. Position of the O-H type Grid of the modified Fruit fly wing (aspect ratio AR=3.74).

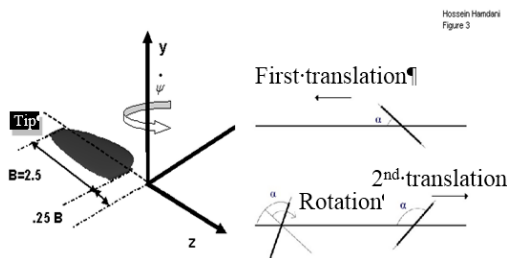


Fig. 3. Motion set up for the Fruit fly wing.

For hovering, the flip motion occurs relative to the translation of the wing. A parameter ADF (ADvance Factor) is introduced to relate the scheduling of a flip motion (τ_r) with the azimuth translation during a stroke and it is expressed as:

$$ADF = \tau_r + \Delta\tau_r - \tau_t \quad (1)$$

where $\Delta\tau_r$ is the total time for the flipping motion; τ_r is the instant at which flipping motion (rotation) commences during the stroke and τ_t is the total time for one stroke, i.e. half cycle ($\tau_t = \tau_a + \Delta\tau_t + \tau_d$), which is set so that the azimuth angle (ψ) during a stroke is affixed at 155° . Here, τ_a and τ_d are the non-dimensional times during which the

acceleration and deceleration in azimuth occurs, respectively and $\Delta\tau_t$ is the non-dimensional time for the constant speed phase of the translation in the azimuth.

ADF (ADvance Factor) essentially provides the value of time at which flipping commences. For instance, ADF= 0.5 implies that half of the flipping motion occurs in Stroke 1 while the other half during Stroke 2 i.e. symmetric flipping. The major parameter for flipping motion is the duration of flipping which is kept constant i.e. $\Delta\tau_r = 1.0$. The translational speed, u_t , is equal to U during the constant speed phase. During the acceleration and deceleration phases, u_t is given by:

$$u_t^+ = -0.5 \left[1 - \cos \left\{ \frac{\pi(\tau - \tau_1)}{\tau_a} \right\} \right]; \quad \tau_1 \leq \tau \leq \tau_a \quad (2)$$

$$u_t^+ = 0.5 \left[1 + \cos \left\{ \frac{\pi(\tau - \tau_2)}{\tau_d} \right\} \right]; \quad \tau_2 \leq \tau \leq \tau_d \quad (3)$$

where, $u_t^+ = \frac{u_t}{U}$, $\tau = \tau U/c$ (equivalent to number of

chord lengths travelled), c is the chord length of the wing and U is a reference velocity. Here Re is also based on c and U and it is 4000. τ_1 and τ_2 are the non-dimensional times at which the acceleration and deceleration start in each stroke, respectively.

Denoting the azimuth rotation speed as $\dot{\psi}$

$$(U = r_2 \dot{\psi}), \text{ where, } r_2 = \left[\int_A r^2 \frac{dA}{A} \right]^{1/2} \text{ (second moment}$$

of wing area) is calculated as $0.58l$, where l is wing span (B) plus the distance between the wing root to the rotational axis ($0.25 B$). During the pitching motion ($\Delta\tau_r$), the wing pitches from $\alpha_m = \alpha^\circ$ to $(180 - \alpha)^\circ$ at an angular velocity whose maximum amplitude (α_o^+) is defined by:

$$\dot{\alpha}^+ = 0.5\alpha_o^+ \left[1 - \cos \left\{ 2\pi(\tau - \tau_r) / \Delta\tau_r \right\} \right]; \quad \tau_r \leq \tau \leq \tau_r + \Delta\tau_r \quad (4)$$

where, $\dot{\alpha}^+ = \dot{\alpha} c / U$, α_o^+ is a constant representing the maximum value of $\dot{\alpha}^+$. During $\Delta\tau_r$, the wing rotates from $\alpha = 40^\circ$ to $\alpha = 140^\circ$; therefore, when either α_o^+ or $\Delta\tau_r$ are specified, the other can be determined by the relation $\alpha_o^+ = (\alpha_{final} - \alpha_{start}) / 0.5\Delta\tau_r$.

The major parameters in the present study are

Table 1 Description of Cases with different ADFs

* ADF = $\tau_r + \Delta\tau_r - \tau_t$ * $\Delta\tau_r = \tau_a + \tau_d = 0.5 + 0.5 = 1.0$ * $\tau_t = 4.91$: time for 1 stroke which includes acceleration, constant speed phase and deceleration * During Stroke 1, deceleration starts at $\tau = 4.41$			
Case	ADF	τ_r (Pitching start instant)	Correspondence of Pitching and Stroke 1 Azimuth deceleration
1	0.5	4.41	Starts with deceleration
2	0.25	4.16	0.25 c before deceleration commences
3	0.0	3.91	0.5 c before deceleration commences
4	-0.25	3.66	0.75 c before deceleration commences
5	1.0	4.91	Starts at the end of Stoke 1 deceleration

Table 2 Mean Force Coefficients: Experimental and Numerical Results for a wing in azimuth rotation after rapid acceleration

AoA α (degrees)	Experimental †		Numerical ($\tau_a = 0.5$)		% Difference in $\overline{C_L}$
	$\overline{C_L}$	$\overline{C_D}$	$\overline{C_L}$	$\overline{C_D}$	
40	1.886	1.55	1.96	1.49	-3.9
30	1.7128	.938	1.72	.904	-0.11
20	1.205	.527	1.24	.429	-2.9
10	.6236	.274	.628	.154	-0.7

† data extracted from Fig. 1A [Birch et.al (2004)] , error in valves ± 0.25

$\tau_a = 0.5, \tau_d = 0.5, \Delta\tau_r = 1.0$ or $\alpha_o^+ = 3.4906$ at $Re = 4000$ and $M_\infty = 0.1$. The motion is continued till approximately the similar mean force coefficients are achieved during the two stroke of a cycle and hence only the final stroke is discussed in the detail. The complete motion's non dimensional time is normalized to a scale of 1 using the cycle time τ_c (which is 9.82).

Table 1 shows the details of the four cases considered in the present study. The last column depicts the flip scheduling with respect to Stroke 1 deceleration. It is important to mention that the cases have been selected in a manner so that at the start of the constant speed phase of the Stroke 2, the angle of attack is about 40° .

In essence, there are five variables while considering the motion: Acceleration time (τ_a), Deceleration time (τ_d), Stroke amplitude (ψ), flip velocity ($\dot{\alpha} = \dot{\alpha}c/U$) and scheduling of the Flipping motion (ADF). In the present study, the following assumptions are made to reduce the number of variables:

- (a) Acceleration and deceleration time are kept equal to $\tau_a = \tau_d = 0.5$.
- (b) Stroke amplitude (ψ) or azimuth angle during a stroke is fixed at 155° , which corresponds to $\tau = 4.91$.

- (c) Flipping velocity ($\dot{\alpha} = \dot{\alpha}c/U$) is given a value such that the wing rotates from $\alpha = 40^\circ$ to $\alpha = 140^\circ$ within $\tau = 1.0$.
- (d) Flipping motion (stroke reversal) is scheduled according to the value of the ADF. A total of 4 cases are considered and the details are presented in Table 2.

4.2 Grid Sensitivity Study

For the Grid independence study, the wing translation starts by accelerating for τ_a in the still air (Eq. 1) to a constant speed U (denoted as Motion 1). Due to this half of the hovering motion (i.e. acceleration and constant speed azimuth rotation only), the grid sensitivity study does not require ADF factor since the stroke reversal (or flip) is not taking place. Mach 0.1 is selected for this study. Two grids are considered: While the Grid 1 is of the size $125 \times 72 \times 76$ in the normal, around the wing section, and the span-wise directions, respectively, whereas the Grid 2 is of $156 \times 90 \times 76$. The far field boundary is set at 10 chord lengths away from the wing surface in the normal direction and 5 chord lengths away from the tip in the span-wise direction. The calculated lift and drag coefficients are shown in Fig. 4.

It is seen that during the acceleration phase, there is almost no difference between the results of these two grids; however, during constant speed phase,

there is a very small difference between the results, which indicates that results of grid 1 and grid 2 are similar. From the above result, grid 2 is selected for the present study for ensuring more accuracy as well as better resolution of the flow structures.

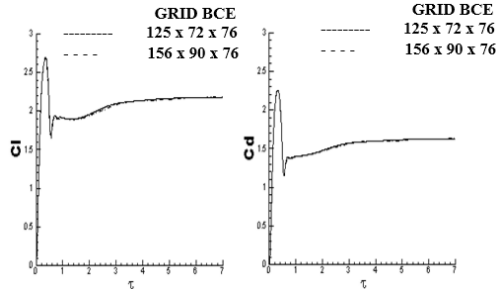


Fig. 4. Lift and Drag force coefficients plots versus τ for Grid 1 and 2.

4.3 Mach Number Sensitivity Study

In order to obtain the solutions close to that of incompressible flow, the value of Mach number needed to be small enough so that the compressibility effects do not affect the solution. For this purpose, the calculations are performed on the wing performing Motion 1. These calculations are performed at three Mach numbers, $M_\infty=0.1, 0.05$ and 0.025 at $Re=4000$. Fig. 5 shows the lift (C_L) and drag (C_D) force coefficients at the different Mach numbers and it is seen that the results for all the three Mach numbers are similar during the acceleration phase.

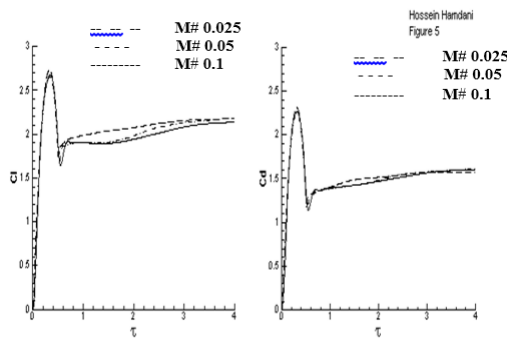


Fig. 5. Force coefficients vs τ for a wing performing Motion 1 at different Mach Numbers.

In the constant speed phase, the lower Mach number gives slightly higher lift coefficient as compared to $M_\infty=0.1$. Therefore, Mach 0.1 (33 ms^{-1}) is selected for the subsequent computations since it would give a good approximation (qualitative) of the incompressible flow at Mach number as low as 0.01 (3.3 ms^{-1}).

5. RESULTS AND DISCUSSION

5.1 Code Validation

The code has been validated by comparing the results with the experimental data at the low

Reynolds number by Hamdani and Sun (2000). The code validation is also performed by comparing the computational results with the experimental at $Re=120$ and 1400 by Birch *et al.* (2004), respectively. Table 2 shows the mean lift and drag coefficients at the different angles of attack for the experimental and computational comparison of the results. Figure 6 shows comparative force coefficient plots for the experimental and numerical results. Essentially, the results are similar especially when α is small. Small variation seen in the results could be due to different acceleration time used in the experiment by Birch *et al.* (2004), which is not known.

5.2 Case 1 (ADF=0.5)

In all the cases, the first cycle commences in the still air with the wing acceleration ($\tau_a=0.5$) at $\alpha=40^\circ$, which is followed by a constant speed azimuth rotation. During the case 1 at $\tau=4.41$, the deceleration starts to bring the wing to halt in the azimuth and simultaneously the wings starts to pitch up. At the end of the deceleration, the pitching rate is maximum and $\alpha=90^\circ$. At this stage, the stroke 1 of the cycle ends. Stroke 2 begins with the acceleration in the azimuth and the pitch motion from $\alpha=90^\circ$ to $\alpha=140^\circ$. At the start of the constant speed phase, the flipping is completed and the wing is moving at $\alpha=140^\circ$ through the wake of the Stroke 1. The Stroke 2 deceleration and flipping starts simultaneously and at the end of the deceleration, the Stroke 2 (and Cycle 1) is completed. The wing continues to perform the motion with the same kinematics as the Cycle 1 and the computations are continued till the results of two the successive strokes are similar. Fig. 7 shows the lift and drag coefficients versus τ/τ_c for the Stroke 4 during the Cycle 2. $\overline{C_L}$ and $\overline{C_D}$ (Weighted average lift and drag coefficients) for the final stroke is 1.35 and 0.79 , respectively giving $\overline{C_L}/\overline{C_D}$ of 1.7 .

The Stroke 4 starts with a low value of $C_L=0.12$. As $\dot{\alpha}$ reduces from a maximum value to zero and $\dot{\psi}$ increases from zero to its maximum value, a peak value of $C_L=1.13$ (Location 1: $\tau/\tau_c=1.52$) is achieved. By the end of the acceleration ($\tau/\tau_c=1.55$), the C_L peak has subsided. During the constant speed translation phase, the lift coefficient increase is steady till $\tau/\tau_c=1.65$. After which, the increase in C_L is gradual and the value of 2.165 (Location 2) is achieved by the end of the constant speed phase. At $\tau/\tau_c=1.95$, the azimuth deceleration and the pitch up rotation starts simultaneously, where the C_L drops to -1.128 (Location 3) at about the mid of this phase (or the point of maximum deceleration rate). It then increases to a value of $C_L=0.12$ (at the end of the stroke *i.e.* the deceleration has finished and $\dot{\alpha}$ is maximum).

On the other hand, C_D is 0.63 at the start of the stroke 4 ($\tau/\tau_c=1.5$) and increases rapidly during the acceleration in the azimuth direction to a peak value of about $C_D=2.0$ ($\tau/\tau_c=1.515$). By the end of the acceleration ($\tau/\tau_c=1.55$), C_D peak has also subsided and for the duration of the constant speed

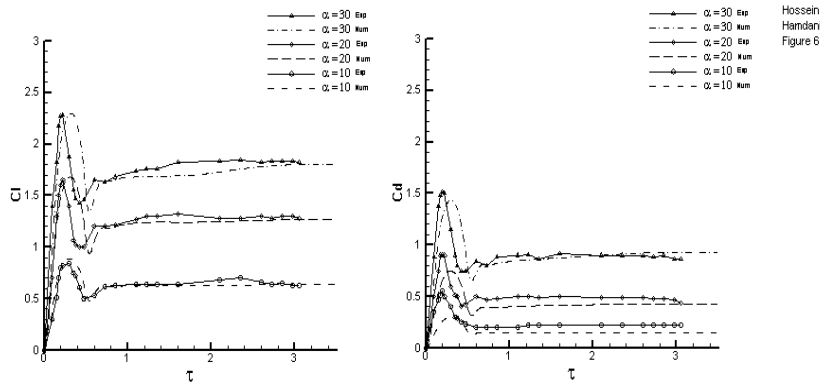


Fig. 6. Experimental (Dickinson *et al*) and Numerical results of the Wing performing Motion 1.

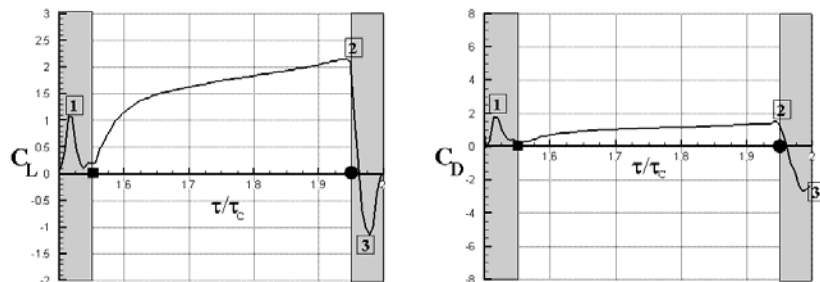


Fig. 7. Case 1 (ADF=0.5). Lift and drag coefficients versus non-dimensional time during Stroke 4. Filled square shows end of acceleration and filled circle start of deceleration in azimuth. Shaded rectangles depict the flipping motion.

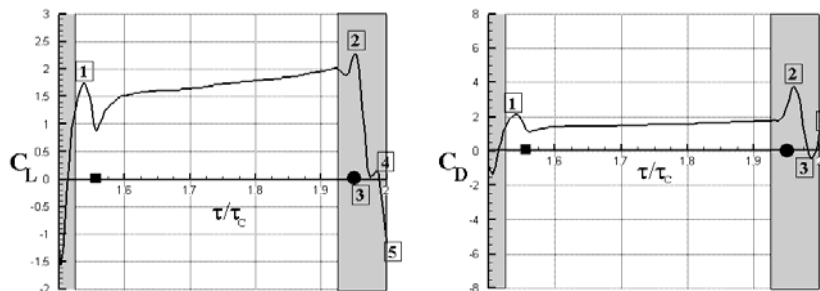


Fig. 8. Case 2 (ADF=0.25). Lift and drag coefficients versus non-dimensional time during Stroke 4. Filled square shows end of acceleration and filled circle start of deceleration in azimuth. Shaded rectangles depict the flipping motion.

translation phase, the drag coefficient increase is steady and a value of 1.6 is achieved by the end of the constant speed phase. At $\tau/\tau_c = 1.95$, the azimuth deceleration and the pitch up rotation starts simultaneously, as the wing angle of attack increases, C_D increases to a peak of 2.65 ($\tau/\tau_c = 1.988$) and by the end of the deceleration phase, has reached 0.63.

5.3 Case 2 (ADF=0.25)

In Case 2, the kinematics is similar to the Case 1, however the flip motion is initiated 0.25 chord length before the deceleration phase of the stroke 1 and ends at the mid of the acceleration phase of the stroke 2.

The stroke begins with a high negative value of C_L (about -1.5) and C_D is about 1.5. During the starting phase, $\dot{\alpha}$ is decreasing to zero while $\dot{\psi}$ is

increasing. As can be seen from Fig. 8, C_L peak value of 1.865 and C_D peak value 2.05 (location 1) is attained during the acceleration phase. By the end of the acceleration phase, ($\tau/\tau_c=1.55$), C_L drops to less than 1.0. During the constant speed translation, C_L gradually increases (due to delayed stall mechanism) and before the flip starts (0.25 c before deceleration); C_L is approximately 1.97, which is higher than the force peak produced during the acceleration phase. Immediately after the flipping commences, a second peak (location 2) of the force coefficients is observed (C_L and C_D is 2.404 and 3.558 respectively). As soon as the deceleration in azimuth starts, the combined effect of the deceleration and pitching ($\dot{\psi}$ and $\dot{\alpha}$) is dominated by the deceleration and the lift reduces sharply (between location 2 and 3). At $\alpha=90^\circ$, the lift coefficient is almost zero (location 3). There is then a slight increase in C_L (location 4); however C_L

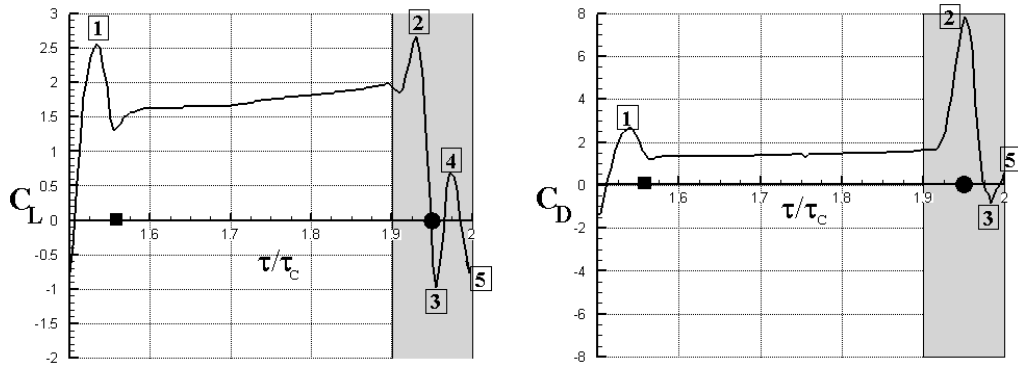


Fig. 9. Case 3 (ADF=0.0). Lift and drag coefficients versus non-dimensional time during Stroke 4. Filled square shows end of acceleration and filled circle start of deceleration in azimuth. Shaded rectangles depict the flipping motion.

drops sharply to a high negative value (location 5) by the end of the stroke under the influence of the deceleration.

In comparison with C_L , C_D shows a similar behavior with a large peak during the acceleration, which is followed by a drag plateau during the constant speed phase. During the flipping motion, another peak is observed (location 2). A negative peak is seen which corresponds nearly to the maximum deceleration rate and towards the end of the stroke ($\alpha > 90^\circ$), C_D has a positive value due to change in the direction of the drag force. $\overline{C_L}$ and $\overline{C_D}$ for the stroke are 1.5 and 1.47, respectively while $\overline{C_L}/\overline{C_D}$ is calculated as 1.02.

5.4 Case 3 (ADF=0.0)

In the Case 3, the kinematics is similar to the Case 1, however the flip motion is initiated 0.5 chord length before the deceleration phase of the stroke 1 and ends with the deceleration phase of the translation. Or, there is no flipping motion during the acceleration phase of the next stroke.

The stroke begins with C_L about -0.9. During the starting phase, α is zero (no flipping motion) while $\dot{\psi}$ is increasing. From Fig. 9, it is seen that qualitatively behavior of the force coefficients is similar to that of the previous case ADF=0.25 (Fig. 8). It is seen that the C_L and C_D peaks (location 1: 2.5 and 2.6 respectively) are produced during the acceleration phase. During the constant speed translation, the forces gradually increase and there is a lift and drag plateau during the most part of azimuth translation (delayed stall mechanism). As the flipping motion starts, C_L increase to about 2.7 (location 2) or a lift peak associated with flipping (rotational lift). As α increases further, C_L starts to decrease and at $\alpha=90^\circ$ (which coincides with start of deceleration and maximum flipping rate); C_L is zero. Under the influence of the deceleration, C_L drops to -1 (location 3) and as the maximum deceleration rate is achieved; a positive peak of $C_L = 0.7$ appears (location 4). C_L drops to a negative value of -0.9 at the end of the stroke. It is worthwhile to note that this spike (location 4) is not evident in the previous two cases; thus highlighting

the importance of the flipping motion scheduling viz deceleration in the azimuth rotation.

In comparison with C_L , C_D shows a similar behavior with the large peak during acceleration, which is followed by a drag plateau during the constant speed phase. During the flipping motion, very high peak is observed corresponding to the maximum flip rate (location 2). During the deceleration, C_D continually decreases and by the end of the stroke, C_D is about -1.25. $\overline{C_L}$ and $\overline{C_D}$ for the stroke are 1.51 and 1.7, respectively while $\overline{C_L}/\overline{C_D}$ is calculated as 0.88.

5.5 Case 4 (ADF=-0.25)

With similar kinematics as the previous cases except that the flip starts 0.75 chords length before the deceleration starts and ends at the mid of the deceleration phase of the stroke ($\alpha=140^\circ$). Therefore, the wing continues to decelerate for the quarter chord length at an angle of attack of 140°

The stroke begins with C_L and C_D value of -0.4 and 0, respectively. At the start of the stroke, α is zero (no flipping motion) while $\dot{\psi}$ is increasing. From Fig. 10, it is seen that qualitatively behavior of the force coefficients is similar to that of the previous case ADF=0.0 (Fig. 9). As the wing starts to accelerate, C_L and C_D start to rise till a force peak is achieved (location 1: 2.88 and 2.77 respectively). There is a sudden decrease in C_L and C_D as the acceleration phase ends.

During the constant speed translation phase, the force coefficients stabilize at a high C_L and C_D value as compared to the steady state results thus signifying the stall absence phenomenon. The flipping motion commences 0.75 chords length travel before the azimuthal deceleration. Due to the flipping motion, C_L increases to about 2.66 (location 2) and thereafter it drops sharply. At the mid of the flipping (flipping rate is maximum and $\alpha=90^\circ$), C_L is zero. As the wing continues to rotate beyond 90° , C_L continues to decrease till location 3 due to the orientation of the lift vector. Shortly beyond location 3, the deceleration starts and C_L attains another peak at the maximum deceleration

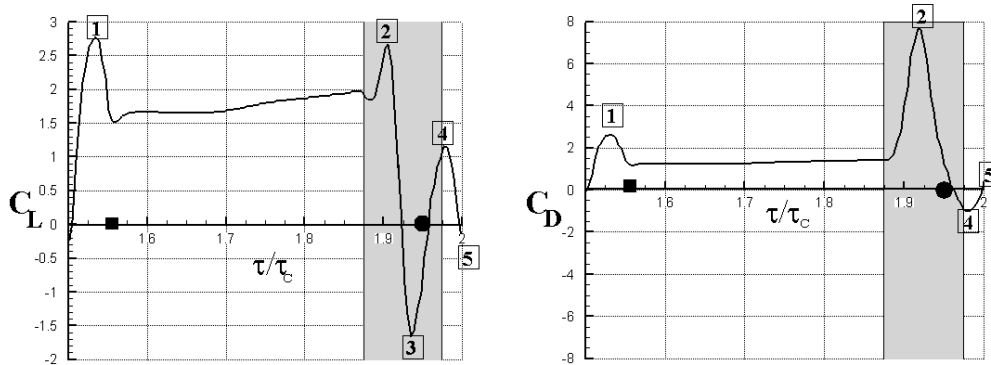


Fig. 10. Case 4 (ADF=0.25). Lift and drag coefficients versus non-dimensional time during Stroke 4. Filled square shows end of acceleration and filled circle start of deceleration in azimuth. Shaded rectangles depict the flipping motion.

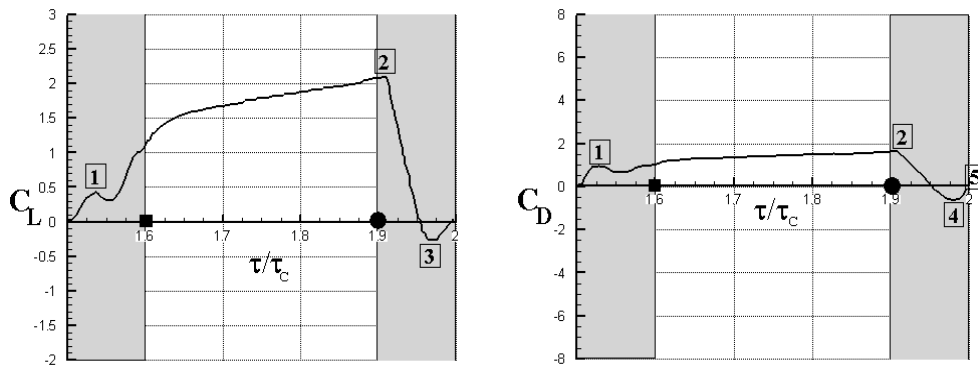


Fig. 11. Case 5 (ADF=1.0). Lift and drag coefficients versus non-dimensional time during Stroke 4. Filled square shows end of acceleration and filled circle start of deceleration in azimuth. Shaded rectangles depict the flipping motion.

rate (location 4: flipping has ended) and similar to the acceleration phase; C_L decreases as the deceleration rate reduces to zero (location 5). It is worthwhile to observe the three positive force peaks (1, 2, 4) and the two negative force peaks (location 3 and 5).

C_D , at the start of the stroke is almost zero and increases to a high value during the acceleration. As the acceleration rate reduces, C_D decreases and maintains almost a constant value during the constant speed translation phase. The flipping motion causes the drag coefficient to increase and a very large value ($C_D = 7.8$) is achieved at the instant when the flipping rate is maximum and $\alpha = 90^\circ$ (location 2). Beyond this instant, it then starts to decrease rapidly and is close to zero when the deceleration starts. At the location 4 (the flipping has ended and the deceleration rate is maximum), C_D is about -1.0. Thereafter, C_D increases to a value of zero by the end of the stroke. $\overline{C_L}$ and $\overline{C_D}$ for the stroke are 1.47 and 1.62, respectively and $\overline{C_L}/\overline{C_D}$ is calculated as 0.91.

5.6 Case 5 (ADF= 1.0)

A variation of the Case 1 is also investigated in which the flipping motion occurs during the deceleration of the Stroke 1 and the acceleration of Stroke 2 (the symmetric flip scheduling). The

rationale behind investigating this case is on the basis of very good performance during the symmetric flip scheduling and it is worthwhile to reduce the acceleration / deceleration rates during the azimuth (and corresponding the decreased flipping rate) for ascertaining their effect. The kinematics remains the same except for $\tau_a = 1.0, \tau_d = 1.0, \Delta\tau_r = 2.0$ or $\alpha_o^+ = 1.745$. The motion is continued till approximately the similar mean force coefficients are achieved during the two strokes of a cycle and hence only the final stroke is discussed in the detail. The complete motion's non dimensional time is normalized to a scale of 1 using the cycle time τ_c (which is 10.82).

The Stroke 4 starts with an almost zero value (Fig. 11) and increases during the acceleration in the azimuth to a peak value of $C_L = 0.43$. By the end of the acceleration ($\tau/\tau_c = 1.6$), C_L is 1.1, which shows that after subsiding, the lift coefficient has started to rise again. Initially, this rise during the constant speed translation phase is steep and then it gradually increases ($\tau/\tau_c = 1.62$ onwards). By the end of the constant speed translation phase ($\tau/\tau_c = 1.90$), C_L is 2.08. At $\tau/\tau_c = 1.90$, the azimuth deceleration and the flipping starts simultaneously, C_L drops to zero at the mid phase and there is a further decrease till -0.28. It then

increases to a value of $C_L = 0.0$ (at the end of the stroke i.e. the deceleration has finished and $\dot{\alpha}$ is maximum).

C_D has a positive value at the start of the stroke ($\tau/\tau_c = 1.5, C_D = 0.115$) and increases during the acceleration phase to a peak value (location 1) of $C_D = 0.9$ ($\tau/\tau_c = 1.53$) after which it decreases slightly. Thereafter, it begins to increase and by the end of the acceleration ($\tau/\tau_c = 1.6$), the C_D is about 1.0. For the duration of the constant speed translation phase, the drag coefficient increase is steady and a value of 1.6 (location 2) is achieved by the end of the constant speed phase. At $\tau/\tau_c = 1.90$, the azimuth deceleration and pitch up rotation starts simultaneously. C_D decreases to a negative peak of -0.765 (location 4). By the end of the deceleration phase, C_D has a magnitude of 0.1.

It is important to note that due to slow acceleration/ deceleration rates, high peaks are not produced (unlike the previous 4 cases). $\overline{C_L}$ and $\overline{C_D}$ for the stroke are 1.28 and 1.06, respectively, which are lesser than the Case1; $\overline{C_L}/\overline{C_D}$ for the stroke is 1.2.

This case ($\tau_c = 10.82, \Delta\tau = 0.185\tau_c, Re = 4000$) has the kinematics closer to Sun and Tang (2002a, 2002b), where they used $\tau_c = 10.82, \alpha = 40^\circ, \Delta\tau = 0.185\tau_c$ and $Re = 136$ and calculated a $\overline{C_L} = 1.2$ for one stroke. This is almost similar to the one calculated for the final stroke of the case 2 i.e. $\overline{C_L} = 1.19$. While in their study on the lift and power requirements for drosophila by Sun and Tang (2002a), $\overline{C_L}$ was calculated as 1.15 for a symmetric motion with the wing at $\alpha = 36.5^\circ$. The results thus, revalidate the initial assumption of the present study that the flow physics at $M_\infty = 0.1$ is essentially similar to $M_\infty = 0.01$ and with these results, the velocity can be estimated to as low as $U_\infty = 0.14 m s^{-1}$ used by Sun and Tang (2002a, 2002b).

5.7 Discussion

The complexity of the motion and its accompanying results (the force coefficients) merits discussion on various aspects of all the above cases for the purpose of gaining useful insights.

First, the coefficient of lift behavior during a stroke is discussed:

- It is seen that as the flip schedule is further away from the acceleration phase, C_L peak increases during the acceleration phase (For $ADF = 0.5$, C_L peak is the lowest while for $ADF = -0.25$, it is the highest).
- C_L peak occurs approximately at a point where the acceleration rate is maximum.
- The extent of drop in C_L during the acceleration phase is almost the same in magnitude for all the 4 cases (Cases 1 to 4).

- After the acceleration phase, C_L starts to rise and within a short period; there is a constant lift plateau with $C_L \approx 2.0$ (i.e. during the constant speed phase due to the delayed stall mechanism).
- The flipping before the start of the deceleration produces a rotational lift peak and as the flip is scheduled nearer to the deceleration; the magnitude of the peak decreases. In the Case 1, when the flip starts simultaneously with the deceleration; there is no rotational lift peak.
- After the rotational (or the flipping) peak, C_L drops sharply due to the increasing α (case 3 and 4).
- At the onset of the deceleration, C_L drops sharply to a negative value. At $\alpha = 90^\circ$, with $C_L \approx 0$ (due to the orientation of the force vector).
- As $\alpha > 90^\circ$ (the obtuse angle and the flip rate is decreasing) and the deceleration has commenced; C_L then starts to increase to a some positive value (the location 4 in Cases 2, 3 and 4) which is the same effect as the acceleration at the acute angle (like beginning of the stroke). The magnitude of the peak at the location 4 is related to the flip rate at that instant. It is important to note that there is no such peak for the Case 1 since the deceleration and the flipping commences simultaneously; and therefore, no rotational lift peak is observed. Beyond the location 4, C_L drops (location 5) and the drop in C_L decreases with the decreasing flip rate.

The coefficient of drag behavior during the stroke is predictable and it is explained as follows:

- During acceleration, C_D peak is around 2.0 for all the cases and there is a lag between the force production and the acceleration rate i.e. C_D peak occurs a little after the maximum acceleration rate.
- At the end of the acceleration, C_D drops and then maintains almost a constant value throughout the constant speed phase.
- For the cases where the flipping commences before the deceleration, C_D increases rapidly to very large positive values. The large value is associated with the flipping and almost coincides with the rotational lift peak (Cases 2, 3 and 4). While in the case 1, the peak is not exhibited since the flipping and deceleration starts simultaneously and under the deceleration effect; the force production due to the flipping is inhibited.
- Beyond the location 4 (C_D peak), C_D drops sharply under the influence of the decreasing flip rate and more prominently, due to the onset of the deceleration.

From the above discussion, it is seen that the commencement of the flipping before the deceleration gives dividend in the lift production; however the drag penalty is quite large. Table 3 shows the weighted average of the force coefficients during the final stroke. The best aerodynamic efficiency is achieved in the case 1,

Table 3 Force coefficient during Stoke 4 for all the cases

CASE	ADF = 0.5 (CASE 1)		ADF = 0.25 (CASE 2)		ADF = 0.0 (CASE 3)		ADF = -0.25 (CASE 4)		ADF = 1 (CASE 5)	
	$\overline{C_L}$	$\overline{C_D}$	$\overline{C_L}$	$\overline{C_D}$	$\overline{C_L}$	$\overline{C_D}$	$\overline{C_L}$	$\overline{C_D}$	$\overline{C_L}$	$\overline{C_D}$
Stroke 4	1.35	0.79	1.5	1.47	1.51	1.71	1.47	1.62	1.28	1.066
$\overline{C_L} / \overline{C_D}$	1.7		1.02		0.88		0.91		1.2	

where the flipping and deceleration starts at the same time. For the Cases 2, 3 and 4; the prominent lift peaks are exhibited, however the associated drag peak causes overall lesser value of the aerodynamic efficiency. Although the case 5 flip scheduling is similar to the Case 1, however, the drag coefficient is more due to the prolonged motion (the flipping from $\alpha=90^\circ$ to 140° during the acceleration and from $\alpha=140^\circ$ to 90° during the deceleration takes place in 1 chord length; while in the Case 1, the same occurs in the 0.5 chord length travel) at the high α . It is pertinent to mention that any further increase of the ADF, i.e. more flipping occurring at the start of the new stroke, would lead to drag penalty since the wing would be translating at the high α (Case 5 exhibits this statement).

For all the cases, it has been computed that the maximum contribution towards $\overline{C_L}$ comes from the constant speed phase of the stroke i.e. the lift contribution is predominantly due to the delayed stall mechanism. While for $\overline{C_D}$, the constant speed phase and the deceleration (coupled with the flipping) combined contributes towards the high value of the drag coefficient.

5.8 Comparison of First and Final Stroke

For the Case 4, the first stroke (started in still air or in other words pure azimuth rotation) is compared to the final stroke (occurs in the wake of the previous strokes). Such an analysis is useful for assessing the wake capture phenomena. In Fig. 12, it is seen that the lift force coefficient generated in the 1st stroke and the final stroke have similar trend with the two interesting observations: -

- (a) The force coefficient behavior during the acceleration and deceleration phase is quantitatively same.
- (b) During the constant speed translation, the lift force coefficients during the final stroke are consistently slightly lower than the first stroke; while the drag coefficient for both the strokes are same.

This implies that the decreased C_L during the constant speed phase is due to the wake from the previous stroke. Interesting to note is that the negative effect of the wake do not influence the fast acceleration / deceleration phases or in other words, the unsteady effect is dominant. In essence, in the flip scheduling considered in the present study, the wake capture phenomenon to enhance the performance is not observed.

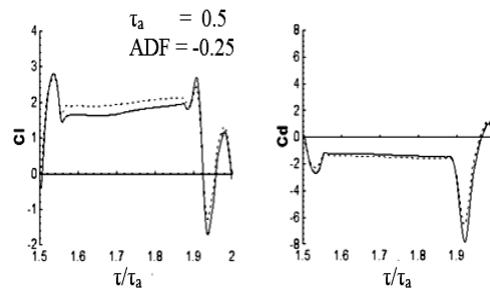


Fig. 12. Case 4: Over lay of force coefficients produced during first (dashed) and final (solid) strokes.

5.9 Vorticity Plots during Case 1

Figures 13, 14, and 15 show the vorticity plots during a stroke for the case 1 i.e. ADF = 0.5. The solid and broken lines represent the positive and negative vorticity lines, respectively. The angle of attack at the beginning of the stroke ($\tau/\tau_c = 1.5$) is 90° . The wing performs a translational acceleration for $\tau_a = 0.5$ toward the right while rotating clockwise from $\alpha \square 90^\circ$ to 140° .

Figure 13 shows the vorticity contours at various span-wise locations during the acceleration phase (i.e. from $\tau/\tau_c=1.5$ to 1.55). The wing is surrounded by the vortices from the previous stroke i.e. the deceleration and flipping from 40° to 90° . Before dilating on the effect of the acceleration on the vortex generation; it is important to partly explain the origin of the vortices from the previous stroke. During the previous stroke, as the wing decelerates, positive and negative vorticity layers are formed on the upper and lower surface of the wing. Simultaneously, the flipping starts which produces new layer of positive vorticity at the upper surface with the existing positive vorticity layer produced during the deceleration. As the wing pitches up, this vortex layer (positive) curls to form the rotation vortex at the leading edge. The positive vorticity at the trailing edge is formed under the negative vorticity layer during the deceleration, which starts to curl form another positive vortex at the trailing edge.

Now as the new Stroke commences, these two positive vortices can be seen detaching as the wing approaches $\alpha = 90^\circ$, especially at the locations closer to the wing-tip. As the wing rotates beyond $\alpha = 90^\circ$ (the pitch down and pitching rate decreases), the negative vorticity layers are produced at the upper and lower surface. As the wing accelerates,

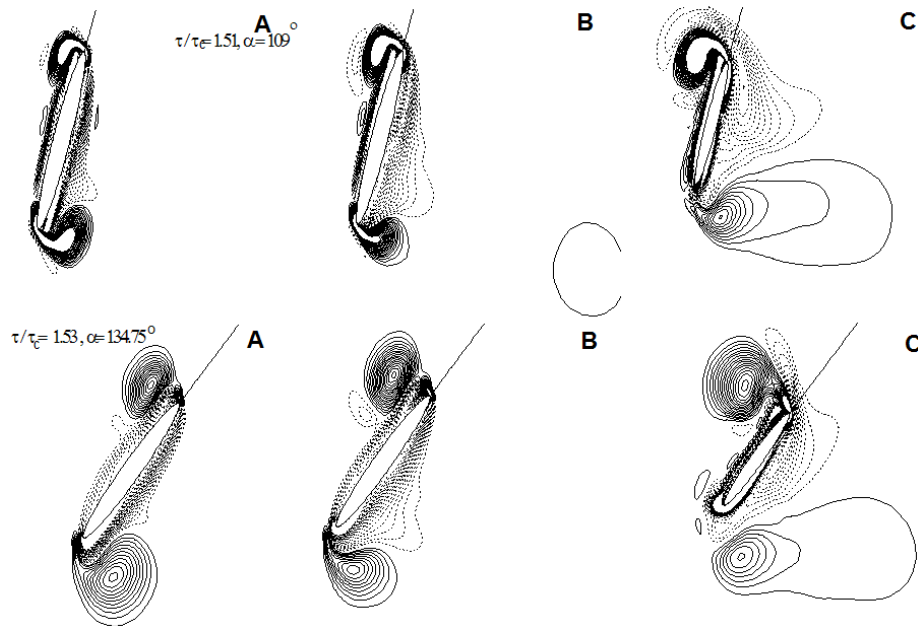


Fig. 13. Case 1: Vorticity plots during acceleration for stroke 4 at different instants. A, B, and C are the 25%, 50%, and 75% span wise locations.

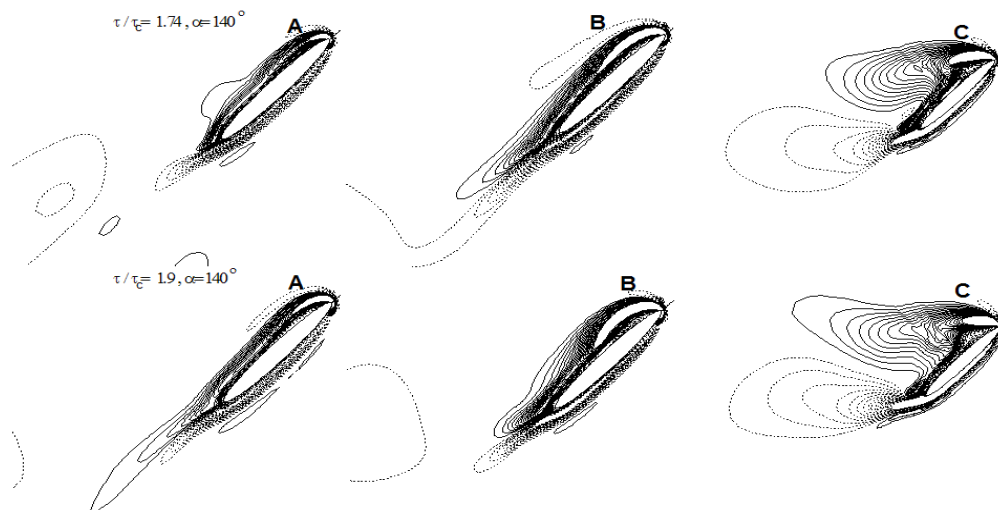


Fig. 14. Case 1: Vorticity plots during constant speed phase for stroke 4 at different instants. A, B, and C are the 25%, 50%, and 75% span wise locations.

the positive vorticity layer is formed on upper surface under the negative vorticity layer and the negative vorticity layer forms on the lower surface. The positive vortices generated during the flip are shed at both the leading and trailing edge locations. The formation of the new vorticity layers during the acceleration occurs in a very short time, which explains (according to vorticity dynamics) the force peak during the acceleration phase.

Figure 14 shows the vorticity plots during the constant speed phase. The negative vorticity on the upper surface at the end of the acceleration (and the flip) accumulates at the trailing edge and sheds at the beginning of the Stroke. During the constant speed phase, the positive vorticity forms the Leading Edge Vortex (LEV) which remains stable.

At the trailing edge, the negative vorticity generated during the flip combines with the negative vorticity produced during the acceleration and this negative vortex (starting vortex) sheds i.e. moves away from the wing causing a gradual rise of the force coefficients. During the constant speed phase, the flow pictures at two the different instants are quite similar; which explains the force coefficients plateau during the most part of the constant speed phase.

Figure 15 shows the vorticity plots during the deceleration phase. The flipping has also commenced where the wing rotates from 40° to 90° . Due to the deceleration, the negative and positive vorticity layers are formed on the upper and lower surface of the wing under the existing vorticity

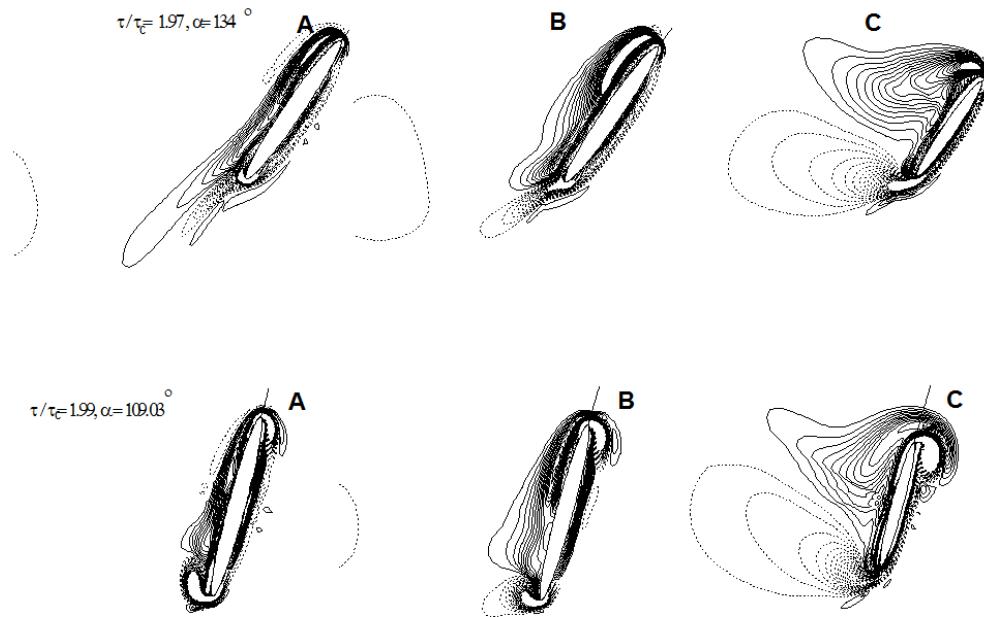


Fig. 15. Case 1: Vorticity plots during deceleration phase for stroke 4 at different instants. A, B, and C are the 25%, 50%, and 75% span wise locations.

layers. Simultaneously, the flipping starts which produces the new layer of the negative vorticity at the upper surface with the existing negative vorticity layer produced during the deceleration. The wing continues to rotate till 90° and the cumulative effect of the deceleration and the flipping causes drop in the force coefficients (similar yet opposite to the acceleration phase). The flow pattern continues to be the same during the subsequent strokes.

7. CONCLUSION

One very interesting aspect from the above results is the diversity of the motion combinations which are available at any point in time, leading to enough lift production to keep an insect (at $Re\ 4000$) in a sustained flight. The flip scheduling is an important parameter and it has the decisive impact on the aerodynamic efficiency during the hovering motion. For all the cases considered in the study (with the different flip scheduling), the lift plateau is observed due to the delayed stall mechanism attributed to the non-shedding of the LEV. During the fast acceleration and deceleration, the large force peaks are achieved due to the unsteady effect, or in other words, due to the generation of the vortices in a very short period of time. In instances where the flip is scheduled before the deceleration, the rotational lift is produced while the accompanying large drag offsets the advantage in the lift production. In a case where the deceleration and the flip starts simultaneously, the rotational lift is not produced; however the absence of the drag penalty due to the flipping results in the large values of $\overline{C_L}/\overline{C_D}$. The wake capture phenomenon is observed but it did not contribute towards the enhancement of the performance, rather the

aerodynamic efficiency is reduced during the subsequent stroke.

REFERENCES

- Aono, H., F. Liang and H. Liu (2008). Near- and far-field aerodynamics in insect hovering flight: an integrated computational study. *Journal of Experimental Biology* 211, 239-257.
- Beam, R. M. and R. F. Warming (1978). An Implicit factored scheme for the compressible Navier-Stokes equations. *AIAA Journal*, 16, 393-402.
- Birch, J. M., W. B. Dickson and M. H. Dickinson, (2004). Force production and flow structure of the leading edge vortex on flapping wings at high and low Reynolds numbers. *J. Exp. Biol.* 207, 1063-1072.
- Bross, M and D. Rockwell (2014). Flow structure on a simultaneously pitching and rotating wing. *J. Fluid Mech* 756, 354-383.
- Dickinson, M. H., F. O. Lehmann And S. SANE (1999). Wing rotation and the aerodynamic basis of insect flight. *Science* 284, 1954-1960.
- Ellington, C. P. (1984a). The aerodynamics of insect flight. I. The quasi-steady analysis, *Philos. Trans. R. Soc. Lond. B Biol. Sci.* 305, 1-15.
- Ellington, C. P. (1984b) The aerodynamics of insect flight. III. *The kinematics*, *Philos. Trans. R. Soc. Lond. B Biol. Sci.* 305, 41-78.
- Ellington, C. P. (1984c). The aerodynamics of insect flight. IV. *Aerodynamic mechanisms*, *Philos. Trans. R. Soc. Lond. B Biol. Sci.* 305, 79-113.

- Ellington, C. P. (1984d). The aerodynamics of insect flight. V. A vortex theory. *Philos. Trans. R. Soc. Lond. B Biol. Sci.* 305, 115-144.
- Ellington, C. P., C. Van De Berg, A. P. Willmott and A. L. R. Thomas (1996). Leading-edge vortices in insect flight. *Nature* 384, 626-630.
- Hamdani, H. and M. Sun (2000). Aerodynamic forces and flow structures of an airfoil in some unsteady motions at low Reynolds number. *Acta Mechanica*, 145(1-4), 1-16.
- Hamdani, H. R. and A. Naqvi (2010). A study on the mechanism of high-lift generation by an insect wing in unsteady motion at small Reynolds number. *International Journal for Numerical Methods in Fluids* 67(5), 581-598.
- Jun-Jiang F., H. Csaba, Q. Hui-He and S. Qei (2014). Effects of aspect ratio on flapping wing aerodynamics in animal flight, *Acta Mechanica Sinica* 30(6), 776-786.
- Lehmann, F. O. (2004a). The mechanisms of lift enhancement in insect flight. *Nature wissenschaften* 91, 10-122.
- Lehmann, F. O. (2004b). Aerial locomotion in flies and robots: kinematic control and aerodynamics of oscillating wings. *Arthropod Struct. Dev.* 33, 331-345.
- Liu, H. (2002). Computational biological fluid dynamics: digitizing and visualizing animal swimming and flying. *Integr. Comp. Biol.* 42, 1050-1059.
- Liu, H. (2005). Simulation-based biological fluid dynamics in animal locomotion. *ASME Appl. Mech. Rev.* 58, 269-282.
- Liu, H. (2005). Simulation-based biological fluid dynamics in animal locomotion. *ASME Appl. Mech. Rev.* 58, 269-282.
- Liu, H. And Kawachi, K. (1998). A numerical study of insect flight. *J. Comput. Phys.* 146, 124-156.
- Liu, H., Ellington, C. P., K. Kawachi, C. VAN DEN BERG and A. P. Willmott (1998). A computational fluid dynamic study of Hawkmoth hovering. *J. Exp. Biol.* 201, 461-477.
- Liu, Y. and M. Sun (2008). Wing kinematics measurement and aerodynamics of hovering Drone flies. *Journal of Experimental Biology* 211, 2014-2025.
- Naderi, A., M. Mojtahedpoor and A. Beiki (2016). Numerical investigation of non-stationary parameters on effective phenomena of a pitching airfoil at low Reynolds number. *Journal of Applied Fluid Mechanics* 9(2), 643-651.
- P. D. Thomas (1982). Composite three-dimensional grids generated by elliptic systems. *AIAA Journal* 20, 1195-1202.
- Sane, S. (2003) The aerodynamics of insect flight. *J. Exp. Biol.* 206, 4191-4208.
- Steger, J. L. (1978). Implicit finite-difference simulation of flow about arbitrary two-dimensional geometries. *AIAA Journal* 16, 679-696.
- Sun, M. and J. Tang (2002a). Lift and power requirements of hovering flight in *Drosophila virilis*. *J. Exp. Biol.* 205, 2413-2427.
- Sun, M. and J. TANG (2002b). Unsteady aerodynamic force generation by a model Fruit fly wing in flapping motion. *J. Exp. Biol.* 205, 55-70.
- Sun, M. and X. Yu (2006). Aerodynamic force generation in hovering flight in a tiny insect. *AIAA J.* 44, 1532-1540.
- Van De Berg, C. and C. P. Ellington (1997a). The three-dimensional leading-edge vortex of a hovering model Hawkmoth. *Philos. Trans. R. Soc. Lond. B Biol. Sci.* 352, 329-340.
- Van De Berg, C. and C. P. Ellington (1997b). The vortex wake of a hovering model Hawkmoth. *Philos. Trans. R. Soc. Lond. B Biol. Sci.* 352, 317-328.
- Wang, Z. J. (2005). Dissecting insect flight. *Annu. Rev. Fluid Mech.* 37, 183-210.
- Wang, Z. J., J. M. Birch and M. H. Dickinson (2004). Unsteady forces and flows in low Reynolds number hovering flight: two-dimensional computations vs. robotic wing experiments. *J. Exp. Biol.* 207, 449-460.
- Wu, J. H. and M. SUN (2004). Unsteady aerodynamic forces of a flapping wing. *J. Exp. Biol.* 207, 1137-1150.
- Yilmaz, T. O, D. Rockwell (2011). Flow structures on finite-span wings due to pitch-up motion. *J Fluid Mech* 691, 518-545.